Fabrication of Homochiral Metal-Organic Framework Membrane for Enantioseparation of Racemic Diols

Kang Huang, Xueliang Dong, Rufei Ren, and Wanqin Jin
State Key Laboratory of Materials-Oriented Chemical Engineering, Nanjing University of Technology, Nanjing 210009, P.R. China

DOI 10.1002/aic.14194
Published online August 12, 2013 in Wiley Online Library (wileyonlinelibrary.com)

Chiral metal-organic frameworks (MOFs) used to discriminate chiral enantiomers are of great practical significance. In this study, a novel homochiral [Ni_2(L-asp)$_2$(bipy)] membrane was fabricated on a porous ceramic support and used for enantioselective separation of racemic diols. High-energy ball milling was applied to decrease the size of MOF crystals to achieve homogeneous seed suspensions. A high-quality homochiral membrane was obtained after optimizing the preparation process. Under the concentration-driven permeation process, racemic 2-methyl-2,4-pentanediol (MPD) was readily separated by the as-prepared membrane. At 30°C, an enantiomeric excess value of 35.5 ± 2.5% was obtained at a feed concentration of 1.0 mmol L^{-1}. The chiral separation of racemic MPD via the membrane followed a preferential sorption mechanism. © 2013 American Institute of Chemical Engineers *AIChE J*, 59: 4364–4372, 2013
Keywords: homochiral, metal-organic frameworks, membrane, chiral separation, racemic diol

Introduction

In the last two decades, metal-organic frameworks (MOFs) have interested many scientists because of their large surface areas, chemically functionalized cavities, flexible skeletons, and intriguing electronic properties. These unique features make them excellent candidates for applications in gas adsorption and storage,[1,2] molecular separation,[3,4] catalysis,[5] sensors,[6] and luminescent devices.[7] More excitingly, functional films and membranes have been developed based on MOF materials, which further extended their applications in the energy and environmental fields.[8–10] MOF membranes have been intensively investigated over the last 4 years for their ability to separate small molecular gases (H_2, CO_2, and hydrocarbons)[11–18] and organic solvents.[19–21]

Recently, a new series of homochiral MOFs has been developed by judicious selection of chiral building blocks and templates.[22–24] As an important subclass of MOF materials, homochiral MOFs have special abilities that include asymmetric catalysis and enantioselective separation via their open chiral channels or cavities.[22–26] A few recent studies further confirm that some homochiral MOFs do exhibit good chiral separation performance.[27–31] A typical homochiral MOF [Zn_2(bdc)(L-lac)(dmf)] was synthesized by Kim and coworkers and used for adsorption separation of racemic sulfoxides,[27] and they obtained enantiomeric excess (*e.e.*) values of 20–27% with the S enantiomer in excess. A better chiral separation performance was obtained on a packed column using this MOF material.[28] It had modest *e.e.* values (7–21%) for enantioselective sorption of racemic alcohols.[29] Cui and coworkers investigated several homochiral MOFs for the separation of racemic alcohols and observed that a homochiral helicate [$Zn_8L_4Cl_8$]·THF·H_2O (THF, Tetrahydrofuran) cage exhibited enantioselectivity for (S)−1-phenylethanol (13.8% *e.e.*) and (S)−1-phenylpropanol (18.6% *e.e.*).[30] The homochiral nanoscale metallacycle [Zn_4($\mathbf{L}_{16}$)$_4$]·4CH_3CN exhibited remarkable sorption for (R)−3-methyl-2-butanol with an *e.e.* value of 99.6%.[31]

These studies give us some indication on how to prepare homochiral MOF membranes for enantioselective separation of chiral compounds. In a recent article, Fischer and coworkers synthesized oriented enantiopure Zn_2(cam)$_2$(dabco) thin films on modified gold substrates.[32] The films were used for enantioselective adsorption instead of membrane separation of racemic 2,5-hexanediol; however, relatively low performance was obtained. In our very recent work, for the first time, a homochiral [Zn_2(bdc)(L-lac)(dmf)] membrane was successfully prepared on a porous ceramic support and used for separating racemic methyl phenyl sulfoxides.[33] Two enantiomers were readily separated by this membrane. Therefore, homochiral MOFs may be useful as a new generation of chiral separation membrane materials.

Considering that most pure enantiomers are used for the synthesis of pharmaceuticals, the separation of biofunctional chiral enantiomers is of great significance. Therefore, the preparation of homochiral MOF membrane containing biologically derived components is preferred. Amino acids are the origin for the functional properties of many extended biological structures, and they are attractive options as chiral building blocks for the synthesis of bioanalogous homochiral MOFs. [Ni_2(L-asp)$_2$(bipy)] (abbreviated as Ni-LAB) is a homochiral MOF synthesized via L-aspartic acid, 4,4'-bipyridine, and Ni cations by Rosseinsky and coworkers.[34] The internal surface of this material is assembled by the amino

Correspondence concerning this article should be addressed to W. Jin at wqjin@njut.edu.cn.

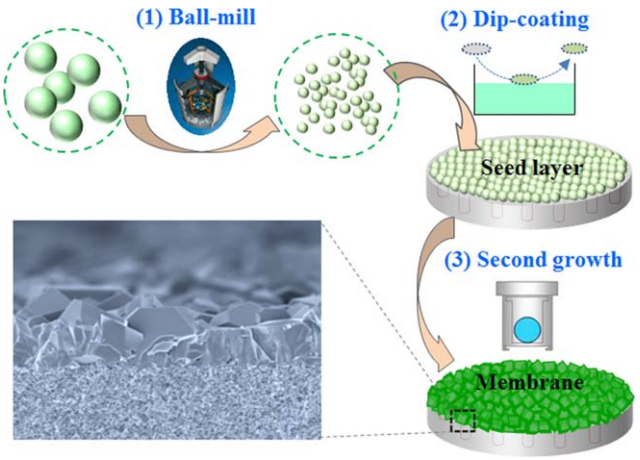

Figure 1. Schematic diagram of the preparation of Ni-LAB membrane.

[Color figure can be viewed in the online issue, which is available at wileyonlinelibrary.com.]

acids (aspartic acids), which provides the chiral sorption sites for the enantioselective separation of diols. Diol enantiomers are useful intermediates for the synthesis of chiral drugs and fine chemicals.[35–37]

In this work, the preparation of Ni-LAB membranes on porous ceramic supports for the separation of racemic MPD was studied. To the best of our knowledge, no MOF membrane has been reported for the purification of chiral diols. For the preparation of integrated MOF membranes, secondary (or seeded) growth has been confirmed as a viable and effective method.[12,13,15–20] A key step for this method is to synthesize suitable seed crystals and a seed layer. However, for many MOF materials, suitable submicron-size seed crystals are not readily available. To address this problem, we applied the high-energy ball-milling method to reduce the size of Ni-LAB crystals mechanically, as shown in Figure 1. After a dip-coating seeding step, the seeded ceramic support was used for membrane formation via a secondary growth step. A high-quality Ni-LAB membrane was obtained after optimizing the preparation process. The as-prepared membrane exhibited good chiral separation performance.

Experimental Details

Materials

Nickel carbonate ($NiCO_3$, Alfa Aesar, 99%), L-aspartic acid (L-asp, Alfa Aesar, 98.5%), 4,4'-bipyridine (bipy, Alfa Aesar, 98%), MPD (Alfa Aesar, 98%), *n*-hexane (C_6H_{14}, 99%), and aluminum oxide (Al_2O_3, 99%) were used without further purification. Methanol (CH_3OH, 99.5%) and deionized water were used as solvents.

Preparation of Ni-LAB powders

Ni-LAB powders were synthesized according to the literature procedure.[34] $NiCO_3$ (0.24 g, 2 mmol) and L-aspartic acid (0.27 g, 2 mmol) were mixed with 15 mL of deionized water (100°C) and stirred for 30 min to form a homogeneous solution. After cooling to room-temperature, 0.31 g of 4,4'-bipyridine (2 mmol) and 15 mL of methanol were added with stirring. The final solution with a molar composition of 1 $NiCO_3$:1 L-asp:1 4,4'-bipyridine:416.5 H_2O:185 CH_3OH was placed in a Teflon-lined stainless steel autoclave (45 mL) and maintained at 150°C for 24 h. After cooling, the solution was centrifuged. Blue-green Ni-LAB powders were obtained after being washed with methanol and dried.

Preparation of -LAB seeds

The prepared Ni-LAB powders with an average particle size of 20–40 μm were ground to submicron-size particles using a high-energy ball mill (PM-100, Retsch India). The milling speed, the ball diameter, and milling time were 450 rpm, 3 mm, and 3 h, respectively. The ball-milled Ni-LAB seeds were used for preparing dip-coating suspensions with various concentrations: 10, 5, and 1 g L^{-1}.

Preparation of Ni-LAB membranes

The Al_2O_3 supports were home-made with an average pore size of ~110 nm and porosity of about 35% as in a previous report.[17] The surfaces of the initial supports were very rough, which made it hard to fabricate continuous Ni-LAB membranes; one side of the support was polished by 1500-mesh SiC sandpaper, washed in deionized water, and then dried in an oven before being used for the growth of MOF membranes.

The Ni-LAB membranes were prepared by a secondary growth method. The polished Al_2O_3 support was seeded with Ni-LAB seeds with the dip-coating method. The Al_2O_3 support was immersed into the Ni-LAB suspension for 20 s, and then dried in an oven overnight at 45°C. During the secondary growth phase, $NiCO_3$ (0.12 g, 1 mmol) and L-aspartic acid (0.13 g, 1 mmol) were mixed with 15 mL of water at 100°C and stirred vigorously for 30 min. After cooling, 0.16 g of 4,4'-bipyridine (1 mmol) and 15 mL of methanol were added and stirred. The seeded support was placed into a Teflon-lined stainless steel autoclave (45 mL) with the seeded side down. The precursor with the molar composition of 1 $NiCO_3$:1 L-asp:1 4,4'-bipyridine:833 H_2O:370 CH_3OH was added and heated to 150°C for 12 h. After cooling, the membrane was washed with methanol and dried at 100°C under vacuum overnight.

Characterizations

The crystal phases of samples were determined by x-ray diffraction (XRD) with Cu Ka radiation (D8 Advance, Bruker). Diffraction patterns were collected at room-temperature in the range of $5° \leq 2\theta \leq 50°$ with a step width of 0.05° and scan rate of 0.2 s $step^{-1}$.

The morphologies of membrane and supports were examined by scanning electron microscopy (SEM; Quanta-200, Philips FEI). The working parameters were: high voltage 20–30 kV, work distance 8–10 mm, and spot 2.0–3.0.

The particle-size distributions and the average particle size of Ni-LAB seeds were analyzed by a particle-size analyzer (NPA152-31A Zetatrac, Microtrac).

The thermal stability of the Ni-LAB powder was analyzed by thermal gravimetric analysis (STA 449 F3, NETZSCH) in the temperature range of 25–800°C with a heating rate of 10°C min^{-1} in a nitrogen atmosphere.

Single-gas permeation experiments were performed on the permeation setup as reported in our previous work.[17] The permeation of small gas molecules (H_2, CH_4, N_2, and CO_2) through Ni-LAB membranes was measured at 25°C. The permeate side was connected with the atmosphere (~0.1 MPa), and the feed side pressure was measured with an exactitude manometer. The penetrated gas flow rate was

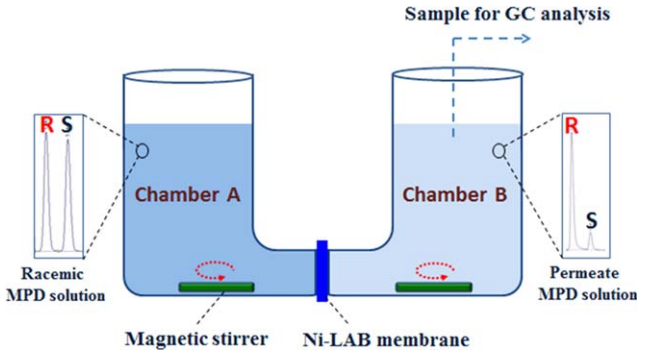

Figure 2. Schematic diagram of the side-by-side diffusion cell used for the measurement of chiral separation performance of Ni-LAB membranes.

[Color figure can be viewed in the online issue, which is available at wileyonlinelibrary.com.]

measured by a soap film flow meter. Ideal selectivity is calculated as the ratio of permeances.

At the steady state, the membrane permeance (F_i) is defined as

$$F_i = \frac{N_i}{\Delta P_i \cdot A} \tag{1}$$

Where N_i is the permeate rate of component i (mol s^{-1}), ΔP_i is the transmembrane pressure difference of i (Pa), and A is the membrane area (m^2).

Chiral sorption

Ni-LAB crystals (0.3 g) were activated at 100°C *in vacuo* for more than 24 h to remove the guest molecules in the channels. The activated crystals were added into a sealed bottle with 3 mL of MPD. The vessel was transferred into a refrigerator at 5°C or an oven at 30°C. After saturation of adsorption (typically for 24 h), the crystals were collected by filtration and washed with a small amount of methanol (10–20 mL) to remove surface-adsorbed guest molecules. The solid was then transferred to another vessel and extracted with *n*-hexane (10 mL). After stirring for 3 h at room-temperature, the extract liquid was collected for gas chromatograph (GC, Shimadzu, model GC-14B, Japan) analysis.

Chiral separation

Chiral separation experiments were conducted on a home-made side-by-side diffusion cell at 30°C. As shown in Figure 2, two chambers that were connected with a clamp serve as the dialyzers. The Ni-LAB membrane was placed between the two chambers and fluororubber gaskets were used to seal the connection. The feed side and the permeate side were continuously stirred by a magnetic stirring apparatus. Racemic MPD that dissolved in the *n*-hexane solvent was introduced to the feed side, whereas the pure *n*-hexane solvent was used at the permeate side. During the permeation experiment, the variation of the MPD concentration at the feed side did not exceed 2%.

All of the samples were derivatized with N-methyl-bis(trifluoroacetamide) (MBTFA, Macherey-Nagel) before analyzing via GC (Shimadzu GC-14B). Typically, 0.5 mL of MBTFA was added to about 2 mg of diol. GC analysis was carried out using a cyclodextrin-based Lipodex-E capillary-GC column (length 25 m, inner diameter 0.25 mm, outer diameter 0.40 mm) supplied by MACHEREY-NAGEL.

The enantiomeric excess (*e.e.*) is determined from the peak areas of the two enantiomers, the *S*-isomer (A_S) and *R*-isomer (A_R)

$$e.e.(\%) = \frac{|A_R - A_S|}{A_R + A_S} \times 100\% \tag{2}$$

The permeation flux of the Ni-LAB membrane can be written as

$$\text{flux} = \frac{n}{A \cdot t} \tag{3}$$

Where n is the permeated enantiomer (mmol), A and t refer to the effective membrane area (m^2) and the permeation time (s), respectively.

Results and Discussions

Preparation of Ni-LAB seeds

The morphology of the as-prepared Ni-LAB particles is shown in Figure 3a. The particle size was about 50 μm. These particles are not suitable to be used as seeds. This is because the seeds can produce nonuniform seed layers on the supports, which result in defects in the Ni-LAB membranes.[38] Therefore, the preparation of Ni-LAB crystals with smaller particle sizes is required. However, it is difficult to control the growth of MOF crystals. Up to now, only a small amount of nanoscale or submicron MOF particles have been prepared.[39,40] In our study, when we used a hydrothermal synthesis method to synthesize the Ni-LAB particles, we tried to vary the concentration of reactants, the synthesis temperature, and time to reduce the particle size, but the synthesized Ni-LAB particles were too large to be suitable for seeding. After these attempts, high-energy ball milling was applied to prepare the submicron-size Ni-LAB seeds. Figure 3b shows the SEM image of the ball-milled Ni-LAB seeds. Obviously, the big Ni-LAB crystals have been ground to be irregular particles with a size of about 1 μm. These particles tended to form clusters, indicating a high surface energy after the ball-milling treatment. In Figure 3c, a single peak around 1 μm is observed for the particle-size distribution of the ball-milled sample, which further confirms the SEM results. Figure 3d shows the XRD patterns of the Ni-LAB seeds before and after the ball-milling treatment. For the ball-milled sample, no obvious change on the crystal structure can be observed except for a light decrease in the intensities of the characteristic peaks. This may be attributed to the breakage of crystals at the grain boundaries and the reduction of the crystallinity. Yang et al.[38] and Kosanović et al.[41] also observed similar results when they prepared zeolite particles using the ball-milling method. The thermogravimetric result of the Ni-LAB powder after activation (without guest molecules) is shown in Figure 4. Ni-LAB has a high thermal stability under 400°C. This is attributed to the extended array of Ni—N and Ni—O bonds within the material.[34]

Preparation of Ni-LAB seed layer

The concentration of the seed suspension has a direct impact on the thickness of the seed layer, and this may affect the bonding strength between the membrane layer and the support as well. Before preparing the Ni-LAB membrane, the concentration of the ball-milled Ni-LAB seed suspension was optimized. For the 10 g L^{-1} seed suspension, as shown

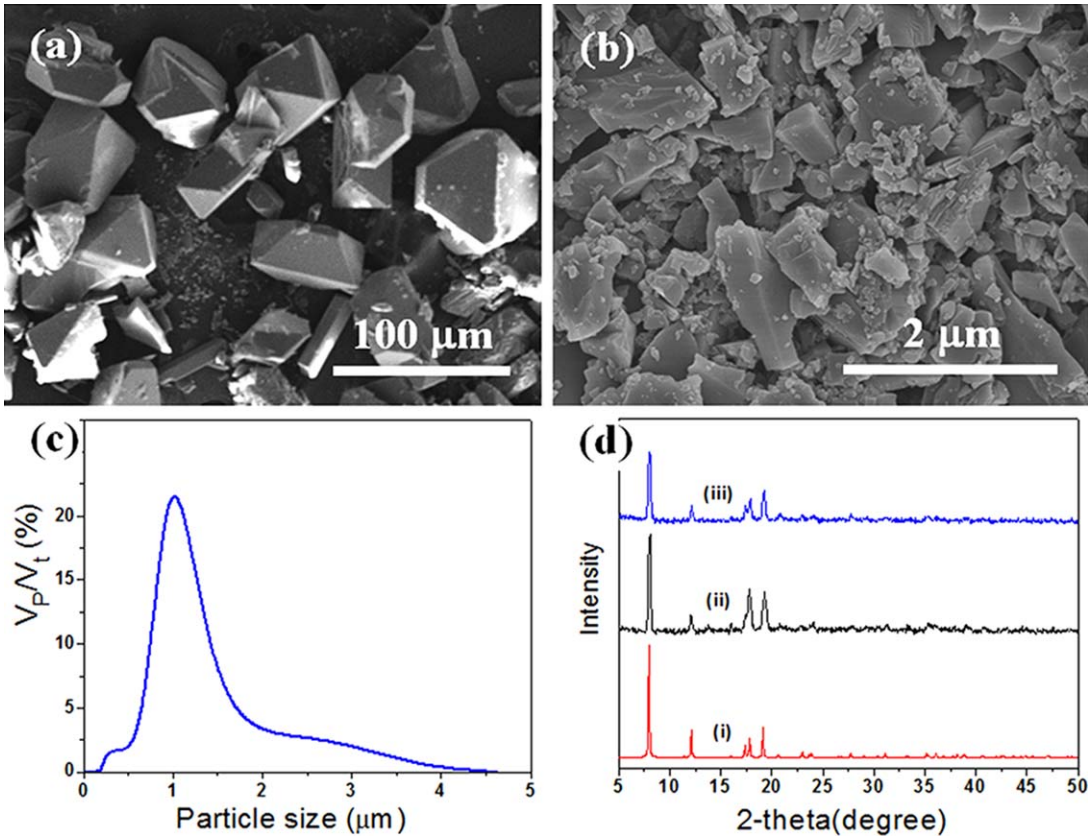

Figure 3. (a) SEM image of as-prepared Ni-LAB particles; (b) SEM image of ball-milled Ni-LAB seeds; (c) the particle-size distributions of the ball-milled sample; (d) the XRD pattern of (i) simulated Ni-LAB crystal diffraction data, (ii) as-prepared Ni-LAB particles, and (iii) ball-milled Ni-LAB seeds.

[Color figure can be viewed in the online issue, which is available at wileyonlinelibrary.com.]

in Figure 5a1, the surface of the seed layer cracked, and the seed layer with a thickness of about 10 μm peeled off from the support (Figure 5a2). By decreasing the concentration of the seed suspension (5 g L^{-1}), the quality of the seed layer is improved (Figures 5b1 and b2). For a 1 g L^{-1} seed suspension, as shown in Figure 5c, the seeds are uniformly distributed on the support, and no cracks are observed. In Figure 5c2, the boundary between the seed layer and support is not obvious, indicating good bonding between them.

To further check the feasibility of preparing seed layers with low-concentration seed suspensions, two Ni-LAB membranes were prepared based on the seed layers using 5 and 1 g L^{-1} suspensions, respectively. The H_2 and N_2 permeation behaviors of these membranes were studied. As shown in Table 1, the H_2/N_2 ideal selectivity of the membrane based on the 1-g L^{-1} seed suspension is better, indicating a higher membrane integrality. Therefore, the 1-g L^{-1} seed suspension was used for the preparation of the Ni-LAB membrane in the following work.

Preparation of Ni-LAB membrane

To prepare a high-quality Ni-LAB membrane, the solvothermal temperature and time were optimized. At low temperatures ($\leq$100°C), the Ni-LAB crystal grew too slowly to form an integrated membrane layer. At relatively high temperatures ($\geq$180°C), however, the fast crystallization of Ni-LAB led to cracking and even peeling of the membrane layer. An optimized solvothermal temperature for preparing the Ni-LAB membrane is 150°C. Additionally, the effect of solvothermal time on the morphology of the membrane was studied. As shown in Figures 6a and b, short synthesis times of 3 and 6 h could not form continuous and high intergrowth Ni-LAB membranes. When the synthesis time is prolonged to 24 h (Figure 6d), the size of the Ni-LAB grains reach about 30 μm and the thickness of the membrane also greatly increases, resulting in relatively low permeances. When the

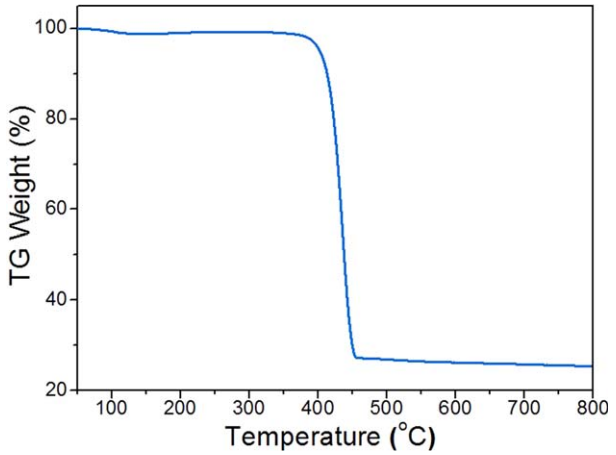

Figure 4. The thermogravimetric result of the Ni-LAB powder in a nitrogen atmosphere with a heating rate of 10°C min^{-1}.

[Color figure can be viewed in the online issue, which is available at wileyonlinelibrary.com.]

Table 1. Effect of Concentration of Seed Suspension on the Properties of As-Prepared Ni-LAB Membranes

Membranes	Concentration (g L^{-1})	Membrane thickness (μm)	H_2 permeances (mol m^{-2} s^{-1} Pa^{-1})	H_2/N_2 ideal selectivity
01	5	25	3.61 × 10−7	2.44
02	1	25	1.93 × 10−7	3.78

synthesis time is 12 h, the surface of the Ni-LAB membrane is free of cracks and covered by grains with an average size of 12 μm, as shown in Figure 6c. A high degree of intergrowth within the Ni-LAB membrane was obtained, and the membrane layer is well-bonded with the support and the thickness of the membrane is about 20 μm (Figure 6e). Energy-dispersive x-ray spectroscopy at the selected area in Figure 6e illustrates that there is a sharp transition between the Ni-LAB layer and the Al_2O_3 support (Figure 6f). Figure 7 shows the XRD pattern of the Ni-LAB seed layer and membrane. For the seed layer, only a weak characteristic peak can be observed, indicating a thin seed layer on the support. In contrast, the XRD pattern of the membrane matches well with the simulation result and is free of impurity phases except for ZnO. The insert is a photograph of the Ni-LAB membrane, which is homogeneous and green.

Gas permeation

To assess the integrity of the prepared Ni-LAB membranes, we tested the permeation of small gas molecules through the Ni-LAB membranes at 25°C. Before gas permeation testing, the as-prepared Ni-LAB membrane was activated at 100°C for 24 h to remove the occluded methanol and H_2O molecules in the Ni-LAB channels. The disk was

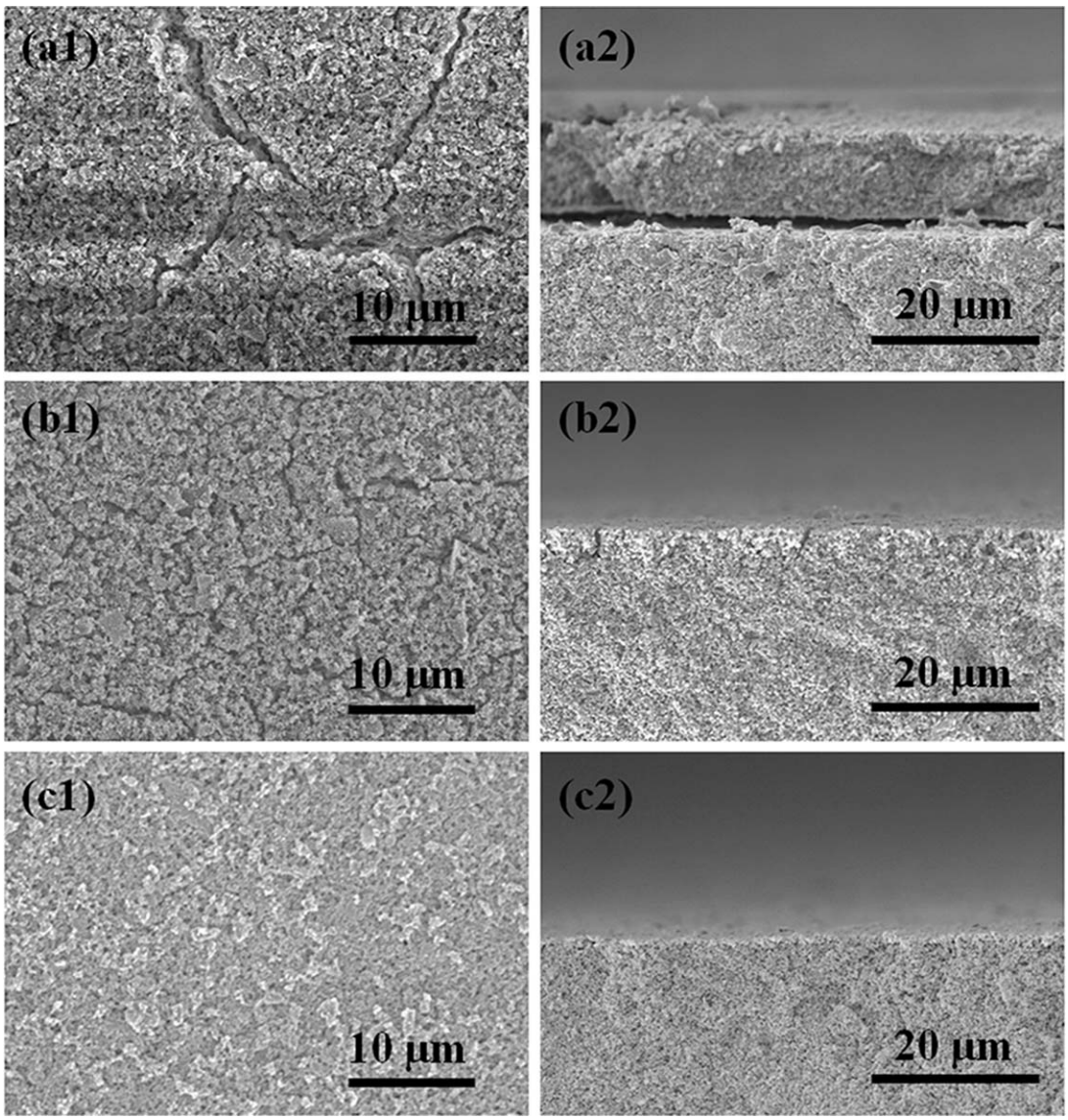

Figure 5. SEM images of seeded supports with different seed concentrations: (a) 10, (b) 5, and (c) 1 g L^{-1}. Top-view (1) and cross-section (2).

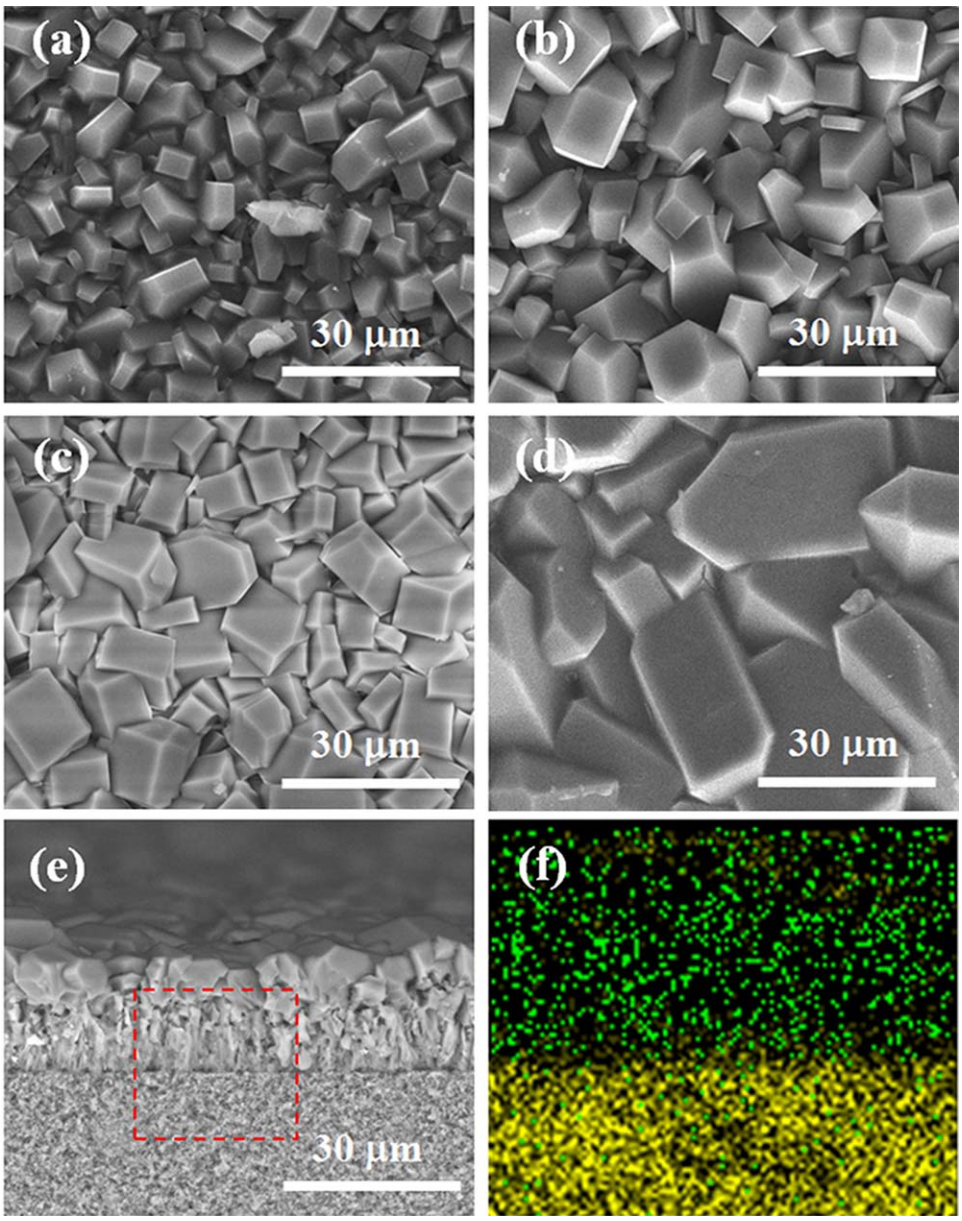

Figure 6. SEM images of Ni-LAB membranes synthesized with different solvothermal times at 150°C: top-view of (a) 3, (b) 6, (c) 12, and (d) 24 h samples; (e) the cross-section of membrane (c); (f) the EDX spectroscopy at a selected area of (e), color code: yellow, Al; green, Ni.

[Color figure can be viewed in the online issue, which is available at wileyonlinelibrary.com.]

sealed in a permeation module with silicone rubber O-rings. The N_2 permeances through the support and the membrane were measured under different transmembrane pressure drops. As shown in Figure 8, the permeance of N_2 through the Al_2O_3 support enhances as the transmembrane pressure drop increases due to the massive contribution of viscous flow to the total flow which arises from the large pore size in the support. Because of the relatively small pore size and porosity, the permeance of the Al_2O_3 support used in this study is lower than the typical values for such types of supports reported in the literature.[42] The permeance of N_2 through the membrane is almost independent of the transmembrane pressure drop, indicating the absence of macroscopic defects.

Figure 9 shows the single-gas permeation results for H_2, CH_4, N_2, and CO_2 through the membrane under a constant transmembrane pressure drop of 0.1 MPa. The permeances of these small gas molecules increase in the order of $CO_2 < N_2 < CH_4 < H_2$. Moreover, the permeances exhibit a linear relationship as the square root of the inversion of their molecular weights increases, indicating that the permeation behaviors of these gas molecules through the Ni-LAB membrane mainly follow the Knudsen diffusion law.[42,43] This further demonstrates that the Ni-LAB membrane is continuous. This result is consistent with the channel size of Ni-LAB. The channels in Ni-LAB have a narrowest cross-section of 3.8 × 4.7 Å, and the upper limit dimension of the guest molecules that can be adsorbed is 4.98 × 6.58 Å. Obviously, the channel size of Ni-LAB is larger than the kinetic diameters of CH_4, N_2, CO_2, and H_2. In addition, amino groups of aspartate molecules have been coordinated with the nickel center,[34] and they had almost no influence on

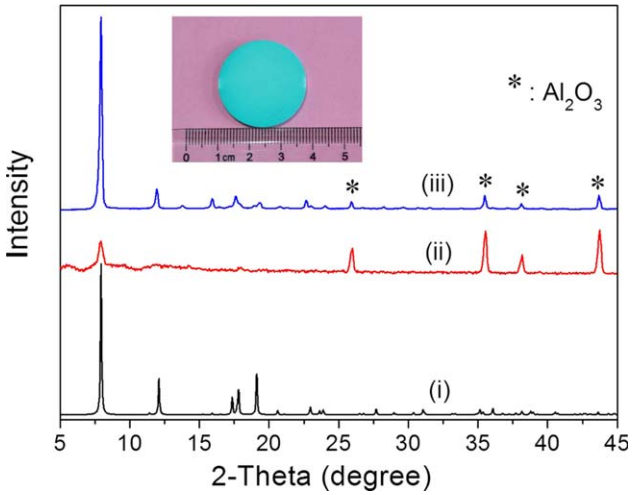

Figure 7. The XRD pattern of (i) simulated Ni-LAB crystal diffraction data, (ii) Ni-LAB seed layer prepared with the 1 g L^{-1} seed suspension, and (iii) Ni-LAB membrane synthesized at 150°C for 12 h.

The insert is a photograph of the Ni-LAB membrane. [Color figure can be viewed in the online issue, which is available at wileyonlinelibrary.com]

the permeation of CO_2. Therefore, the diffusion of these small gas molecules through the membrane follows the Knudsen diffusion law instead of the molecular sieving mechanism.

Chiral separation

The Ni-LAB crystals exhibit enantioselective sorption of chiral diols, such as 1,3-butanediol, 1,2-pentanediol, 2,4-pentanediol, and MPD, because of the chiral adsorption sites in the channels.[34] In this work, racemic MPD was used to measure the chiral separation performance. Before separation tests, the adsorptions of racemic MPD onto the Ni-LAB crystals at 5 and 30°C were measured. The results are listed

Table 2. Sorption of Racemic MPD by Ni-LAB[a]

Temperature (°C)	Adsorption time (*h*)	e.e.%[b]
5	24	73.5 ± 2.5
30	24	42.4 ± 2.0

[a]The e.e. value of racemic MPD is 0.23%.
[b]The e.e. values of R enantiomer over S enantiomer.

in Table 2. Ni-LAB shows preferential sorption for (R)-MPD (R-MPD) over S-MPD. Generally, the amount of sorption increases as the temperature decreases. At relatively low temperatures, the sorption abilities of both R-MPD and S-MPD improve. However, a higher *e.e.* value is obtained, indicating that a low temperature is best for sorption separation.

When a Ni-LAB membrane was used for chiral separation, this process was driven by the concentration difference across the membrane. As shown in Figure 10, the concentrations of the R-MPD and S-MPD at the permeate side increase as the dialysis time increases. After about 8 h, steady-state permeation is reached and linear increases in the enantiomer concentrations are observed. The permeation rate of R-MPD through the Ni-LAB membrane is higher than that of S-MPD. This is consistent with the sorption result. Therefore, we can speculate that the chiral separation of racemic MPD via the Ni-LAB membrane follows a preferential sorption mechanism. During the separation process, more R-MPD can be adsorbed onto the surface of feed side of the membrane and enter into the channel, which increases the concentration gradient of R-MPD across the membrane, resulting in the high permeation rate. This mechanism is further confirmed by a recent simulation work,[44] in which the adsorption behavior of racemic 2,4-pentanediol on the Ni-LAB crystal was simulated. It is reported that S-2,4-pentanediol can only adsorb onto the Ni-LAB crystal at special channel sites with specific conformations that match with its space structure. In contrast, R-2,4-pentanediol can adopt more channel conformations. Therefore, the saturated adsorption amount of the R enantiomer is higher than that of the S enantiomer. However, for membrane separation, the

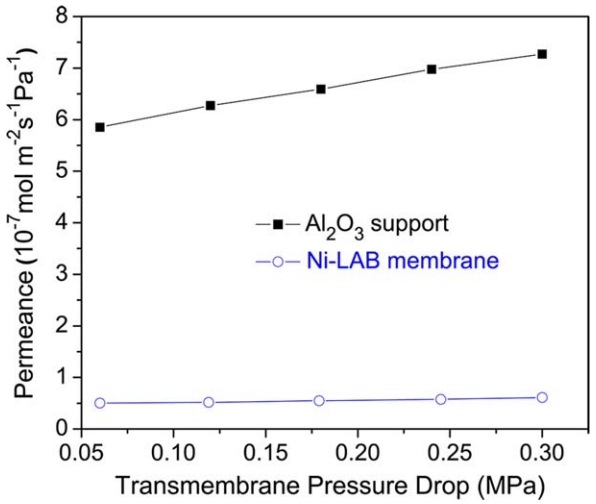

Figure 8. Permeance of nitrogen through the Al_2O_3 support and homochiral Ni-LAB membrane under different transmembrane pressure drops at 25°C.

[Color figure can be viewed in the online issue, which is available at wileyonlinelibrary.com.]

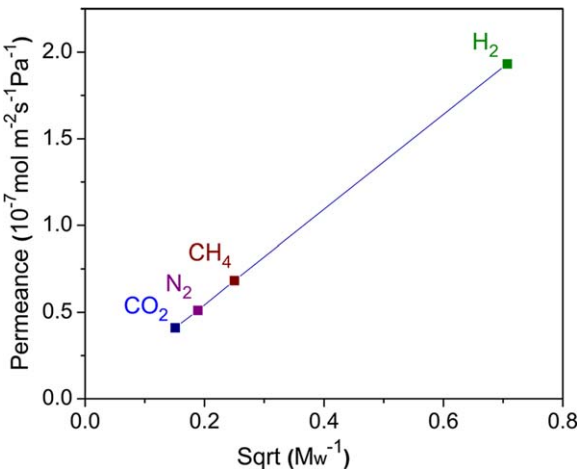

Figure 9. The single gas permeation results of H_2, CH_4, N_2, and CO_2 through the membrane under a constant transmembrane pressure drop of 0.1 MPa at 25°C.

[Color figure can be viewed in the online issue, which is available at wileyonlinelibrary.com.]

permeance depends not only on solubility (or sorption ability) of the membrane but also on the diffusivity in the channels (or pores).[12,45] From Figure 10, after 24-h permeation, the *e.e.* value of R-MPD vs. S-MPD is $35.5 \pm 2.5\%$, which is lower than the sorption result ($42.4 \pm 2\%$). This difference may be caused by S-MPD having a slightly higher diffusivity compared to R-MPD in the channels of Ni-LAB. The simulated pure 2,4-pentanediol enantiomer adsorption isotherms in Ni-LAB also show that the uptake of S-MPD reaches saturation more quickly.[44]

Figure 11 shows the effect of feed concentration on the chiral separation performance of the Ni-LAB membrane. As the concentration of racemic MPD in the feed side increases from 1 to 20 mmol L^{-1}, the *e.e.* value of the permeate product decreases somewhat, whereas the permeation flux increases greatly. The high permeation flux results from the large concentration gradient of racemic MPD across the membrane. However, the high concentration of racemic MPD in the feed side means more MPD molecules come into contact with the membrane surface and occupy the channels, leading to a low discrimination capability of the membrane because the preferential sorption effect declines. In view of this, a low feed concentration is beneficial for the chiral separation in spite of a small permeation flux. Furthermore, to identify the effect of the Al_2O_3 support, we measured its baseline performance under the same conditions. The results indicated that home-made Al_2O_3 supports did not exhibit any chiral separation performance and its effect may be negligible.

Conclusions

A new high-quality chiral Ni-LAB membrane was successfully synthesized on a porous aluminum oxide support by a secondary growth technique. High-energy ball milling is an effective method to prepare submicron-size seeds. The concentration of the seed suspension is a key factor for preparing a continuous and thin seed layer. To prepare an integrated Ni-LAB membrane, the optimization of the solvothermal temperature and time is necessary. The permeation of small gas molecules through the membrane follows Knudsen diffusion law, whereas the chiral separation of racemic MPD via the membrane follows a preferential sorption mechanism. The Ni-LAB membrane exhibits good separation performance for R-MPD. Low-temperature and low-feed concentration are beneficial for obtaining high *e.e.* values. In this work, the highest *e.e.* value of $35.5 \pm 2.5\%$ was obtained at a feed concentration of 1.0 mmol L^{-1} at 30°C. Considering the latest development in chiral MOF materials and advanced techniques in membrane separation, chiral MOF membranes have potential uses in enantioselective separation applications in the future.

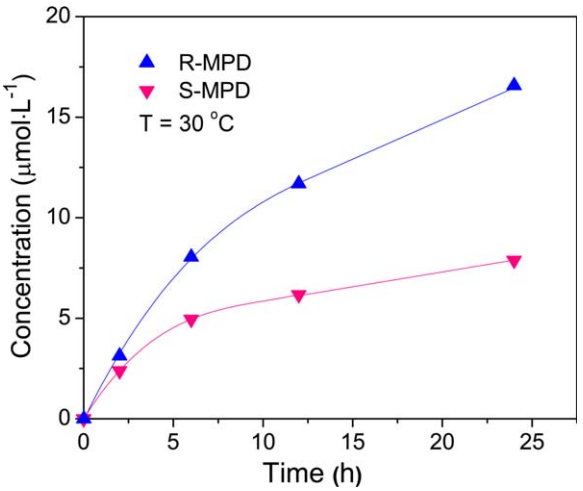

Figure 10. R-MPD and S-MPD concentrations at the permeate side of the Ni-LAB membrane as a function of dialysis time at 30°C.

The initial concentration of racemic MPD on the donor side was 1 mmol L^{-1} with an *e.e.* value of 0.23. [Color figure can be viewed in the online issue, which is available at wileyonlinelibrary.com]

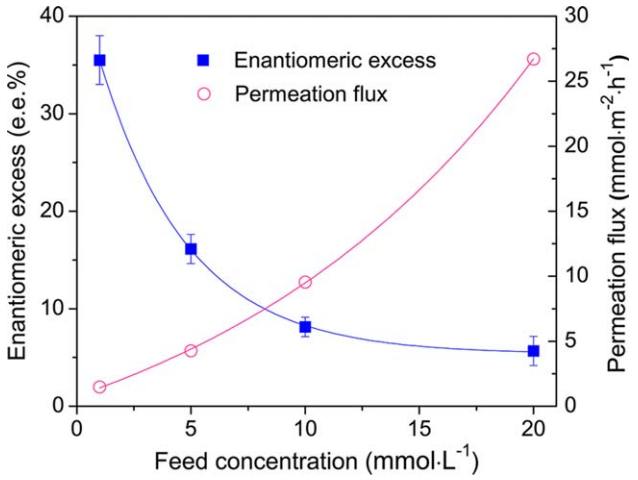

Figure 11. The chiral separation performance of the Ni-LAB membrane under different feed concentrations at 30°C for 24 h.

[Color figure can be viewed in the online issue, which is available at wileyonlinelibrary.com.]

Acknowledgments

Financial supports from the National Natural Science Foundation of China (no. 21176115) and the National Basic Research Program of China (no. 2009CB623406) are gratefully acknowledged. X.L. Dong is grateful for the financial support from the National Natural Science Foundation of China (no. 21006047).

Literature Cited

1. Murray LJ, Dincă M, Long JR. Hydrogen storage in metal–organic frameworks. *Chem Soc Rev*. 2009;38:1294–1314.
2. Sumida K, Rogow DL, Mason JA, McDonald TM, Bloch ED, Herm ZR, Bae TH, Long JR. Carbon dioxide capture in metal-organic frameworks. *Chem Rev*. 2012;112:724–781.
3. Li JR, Kuppler RJ, Zhou HC. Selective gas adsorption and separation in metal-organic frameworks. *Chem Soc Rev*. 2009;38:1477–1504.
4. Li JR, Sculley J, Zhou HC. Metal-organic frameworks for separations. *Chem Rev*. 2012;112:869–932.
5. Corma A, García H, Xamena FXLI. Engineering metal-organic frameworks for heterogeneous catalysis. *Chem Rev*. 2010;110:4606−4655.
6. Kreno LE, Leong K, Farha OK, Allendorf M, Van Duyne RP, Hupp JT. Metal-organic framework materials as chemical sensors. *Chem Rev*. 2012;112:1105–1125.
7. Cui YJ, Yue YF, Qian GD, Chen BL. Luminescent functional metal-organic frameworks. *Chem Rev*. 2012;112:1126–1162.
8. Bradshaw D, Garai A, Huo J. Metal-organic framework growth at functional interfaces: thin films and composites for diverse applications. *Chem Soc Rev*. 2012;41:2344–2381.

9. Betard A, Fischer RA. Metal-organic framework thin films: from fundamentals to applications. *Chem Rev*. 2012;112:1055–1083.
10. Shah M, McCarthy MC, Sachdeva S, Lee AK, Jeong HK. Current status of metal-organic framework membranes for gas separations: promises and challenges. *Ind Eng Chem Res*. 2012;51:2179–2199.
11. Bux H, Liang FY, Li YS, Cravillon J, Wiebcke M, Caro J. Zeolitic imidazolate framework membrane with molecular sieving properties by microwave-assisted solvothermal synthesis. *J Am Chem Soc*. 2009;131:16000–16001.
12. Zhao ZX, Ma XL, Li Z, Lin YS. Synthesis, characterization and gas transport properties of MOF-5 membranes. *J Membr Sci*. 2011;382: 82–90.
13. Venna SR, Carreon MA. Highly permeable zeolite imidazolate framework-8 membranes for CO2/CH4 separation. *J Am Chem Soc*. 2010;132:76–78.
14. Zhang C, Dai Y, Johnson JR, Karvan O, Koros WJ. High performance ZIF-8/6FDA-DAM mixed matrix membrane for propylene/propane separations. *J Membr Sci*. 2012;389:34–42.
15. Pan YC, Li T, Lestari G, Lai ZP. Effective separation of propylene/propane binary mixtures by ZIF-8 membranes. *J Membr Sci*. 2012; 390–391:93–98.
16. Pan YC, Wang B, Lai ZP. Synthesis of ceramic hollow fiber supported zeolitic imidazolate framework-8 (ZIF-8) membranes with high hydrogen permeability. *J Membr Sci*. 2012;421–422:292–298.
17. Hu YX, Dong XL, Nan JP, Jin WQ, Ren XM, Xu NP, Lee YM. Metal-organic framework membranes fabricated via reactive seeding. *Chem Commun*. 2011;47:737–739.
18. Dong XL, Huang K, Liu SN, Ren RF, Jin WQ, Lin YS. Synthesis of zeolitic imidazolate framework-78 molecular-sieve membrane: defect formation and elimination. *J Mater Chem*. 2012;22:19222–19227.
19. Dong XL, Lin YS. Synthesis of an organophilic ZIF-71 membrane for pervaporation solvent separation. *Chem Commun*. 2013;49:1196–1198.
20. Diestel L, Bux H, Wachsmuth D, Caro J. Pervaporation studies of n-hexane, benzene, mesitylene and their mixtures on zeolitic imidazolate framework-8 membranes. *Microporous Mesoporous Mater*. 2012;164:288–293.
21. Liu XL, Li YS, Zhu GQ, Ban YJ, Xu LY, Yang WS. An organophilic pervaporation membrane derived from metal-organic framework nanoparticles for efficient recovery of bio-alcohols. *Angew Chem Int Ed*. 2011;50:10636–10639.
22. Kim K, Banerjee M, Yoon M, Das S. Chiral metal-organic porous materials: synthetic strategies and applications in chiral separation and catalysis. *Top Curr Chem*. 2010;293:115–153.
23. Liu Y, Xuan WM, Cui Y. Engineering homochiral metal-organic frameworks for heterogeneous asymmetric catalysis and enantioselective separation. *Adv Mater*. 2010;22:4112–4135.
24. Nickerl G, Henschel A, Grünker R, Gedrich K, Kaskel S. Chiral metal-organic frameworks and their application in asymmetric catalysis and stereoselective separation. *Chem Ing Tech*. 2011;83:90–103.
25. Ma LQ, Abney C, Lin WB. Enantioselective catalysis with homochiral metal-organic frameworks. *Chem Soc Rev*. 2009;38:1248–1256.
26. Yoon M, Srirambalaji R, Kim K. Homochiral metal-organic frameworks for asymmetric heterogeneous catalysis. *Chem Rev*. 2012;112: 1196–231.
27. Dybtsev DN, Nuzhdin AL, Chun H, Bryliakov KP, Talsi EP, Fedin VP, Kim K. A homochiral metal-organic material with permanent porosity, enantioselective sorption properties, and catalytic activity. *Angew Chem Int Ed*. 2006;45:916–920.
28. Nuzhdin AL, Dybtsev DN, Bryliakov KP, Talsi EP, Fedin VP. Enantioselective chromatographic resolution and one-pot synthesis of enantiomerically pure sulfoxides over a homochiral Zn-organic framework. *J Am Chem Soc*. 2007;129:12958–12959.
29. Suh K, Yutkin MP, Dybtsev DN, Fedin VP, Kim K. Enantioselective sorption of alcohols in a homochiral metal-organic framework. *Chem Commun*. 2012;48:513–515.
30. Xuan WM, Zhang MN, Liu Y, Chen ZJ, Cui Y. A chiral quadruple-stranded helicate cage for enantioselective recognition and separation. *J Am Chem Soc*. 2012;134:6904−6907.
31. Li G, Yu W, Ni J, Liu T, Liu Y, Sheng E, Cui Y. Self-assembly of a homochiral nanoscale metallacycle from a metallosalen complex for enantioselective separation. *Angew Chem Int Ed*. 2008;47:1245–1249.
32. Liu B, Shekhah O, Arslan HK, Liu JX, Wöll C, Fischer RA. Enantiopure metal–organic framework thin films: oriented SURMOF growth and enantioselective adsorption. *Angew Chem Int Ed*. 2012; 51:807–810.
33. Wang WJ, Dong XL, Nan JP, Jin WQ, Hu ZQ, Chen YF, Jiang JW. A homochiral metal-organic framework membrane for enantioselective separation. *Chem Commun*. 2012;48:7022–7024.
34. Vaidhyanathan R, Bradshaw D, Rebilly JN, Barrio JP, Gould JA, Berry NG, Rosseinsky MJ. A family of nanoporous materials based on an amino acid backbone. *Angew Chem Int Ed*. 2006;118: 6645–6649.
35. Choudary BM, Chowdari NS, Madhi S, Kantam ML. A trifunctional catalyst for the synthesis of chiral diols. *Angew Chem Int Ed*. 2001; 40:4619–4623.
36. Wei WL, Wu L, Xu C, Ren JS, Qu XG. A general approach using spiroborate reversible cross-linked Au nanoparticles for visual high-throughput screening of chiral vicinal diols. *Chem Sci*. 2013;4:1156–1162.
37. Nagarapu L, Paparaju V, Satyender A, Bantu R. Total synthesis of (+)-varitriol via a symmetrical furanose diol as the key intermediate. *Tetrahedron Lett*. 2011;52:7075–7078.
38. Yang ZZ, Liu YM, Yu CL, Gu XH, Xu NP. Ball-milled NaA zeolite seeds with submicron size for growth of NaA zeolite membranes. *J Membr Sci*. 2012;392–393:18–28.
39. Cravillon J, Munzer S, Lohmeier SJ, Feldhoff A, Huber K, Wiebcke M. Rapid room-temperature synthesis and characterization of nanocrystals of a prototypical zeolitic imidazolate framework. *Chem Mater*. 2009;21:1410–1412.
40. Pan YC, Liu YY, Zeng GF, Zhao L, Lai ZP. Rapid synthesis of zeolitic imidazolate framework-8 (ZIF-8) nanocrystals in an aqueous system. *Chem Commun*. 2011;47:2071–2073.
41. Kosanović C, Čižmek A, Subotić B, Šmit I, Stubičar M, Tonejc A. Mechanochemistry of zeolites: part 3. Amorphization of zeolites ZSM-5 by ball milling. *Zeolites*. 1995;15:51–57.
42. Liu YY, Ng ZF, Khan EA, Jeong HK, Ching CB, Lai ZP. Synthesis of continuous MOF-5 membranes on porous alpha-alumina substrates. *Microporous Mesoporous Mater*. 2009;118:296–301.
43. Kanezashi M, O'Brien-Abraham J, Lin YS. Gas permeation through DDR-type zeolite membranes at high temperatures. *AIChE J*. 2008; 54:1478−1486.
44. Moghadam PZ, Duüren T. Origin of enantioselectivity in a chiral metal-organic framework: a molecular simulation study. *J Phys Chem C*. 2012;116:20874−20881.
45. Zhang C, Lively RP, Zhang K, Johnson JR, Karvan O, Koros WJ. Unexpected molecular sieving properties of zeolitic imidazolate framework-8. *J Phys Chem Lett*. 2012;3:2130–2134.

Manuscript received Mar. 5, 2013, and revision received July 1, 2013.